Measurement Optimization for Orientation Tracking Based on No Motion No Integration Technique

Measurement Optimization for Orientation Tracking based on No Motion No Integration Technique

Minh Long Hoang, Salvatore Dello Iacono, Vincenzo Paciello, *Senior Member, IEEE*,
Antonio Pietrosanto, *Senior Member, IEEE*
Department of Industrial Engineering
University of Salerno
Fisciano (SA), Italy
{mhoang, sdelloiacono, vpaciello, apietrosanto}@unisa.it

***Abstract*—The main goal of the paper is to fully explore the capability of the 'No Motion No Integration' (NMNI) technique for the optimization of Euler angles in orientation tracking. The gyroscope is the critical component in the Inertial Measurement Unit for angle detection in Industry 4.0. An upgraded NMNI model is introduced to remove the drift of the gyroscope significantly for the advanced measurement approach for roll, pitch, and yaw. A model of threshold update is implemented into the NMNI algorithm to compensate for the increased offset of temperature. This pre-processing method is applied to the Madgwick filter and Mahony filter to acquire the optimal performance. The experiments were carried out by using a low-cost platform equipped with Micro-Electro-Mechanical system sensors. A pan-tilt unit with high accurate positioning was used to move the sensors and obtain a reference angle during both static and dynamic experiments. A substantial improvement was clearly demonstrated after the optimization process. The measurements of Euler angles have minimized noise and tracks around the reference points properly. The results show strong competition from both fusion filters where the fused Mahony accomplishes more stable less variation in roll and pitch, but the fused Madgwick shows more precision in heading/yaw estimation.**

***Index Terms*—Sensor Fusion, Micro Electro Mechanical System (MEMS), Inertial Measurement Unit (IMU), Heading, Orientation, Madgwick filter, Mahony filter, Accelerometer, Gyroscope, Magnetometer.**

I. Introduction

The advancing technology for orientation tracking [1]–[3] has been developing dramatically for the wide-range application in the Industry 4.0, especially in automation [4], [5] and industrial safety [6]–[8]. Micro Electro Mechanical System (MEMS) gyroscope [9]–[12] with angular rate contributes multi-function tasks in the angle measurement such as noise removal for accelerometer or distortion compensation for magnetometer [13]–[15].

Roll, pitch, and yaw are the three positioning parameters, as illustrated in Fig. 1, which has suffered many challenges from drift, noise, and accuracy demand. There are some popular algorithms of sensor fusion which has positively obtained an excellent quality of angle detection like Madgwick and Mahony [16]–[18]. Both filters work on the converted quaternion based on gyroscope data and get drift compensation from the accelerometer and magnetometer. However, the negative impact of noise on the accelerometer and iron distortion on the magnetometer reduces result quality considerably. Hence, the No Motion No Integration (NMNI) technique brings the best characteristic out of gyroscope since no single portion of drift can occur on gyroscope when the sensor is stationary. This pre-processing method worked successfully as described in [19]; its stability overcomes the traditional Madgwick in heading estimation. No transient happens in the proposed system. Continue to that success; this project applies the NMNI algorithm to roll and pitch to observe whether this technique can optimize the tracking ability in inclination conditions. Moreover, a threshold update model is added to the NMNI system for long-term performance where the sensor temperature becomes higher, causing an increase of offset in the gyroscope.

The effectiveness of new fusion filters is verified by high precise reference, located by PTU-C46 (Pan Tilt Unit). In the previous work, the static test and dynamic test on heading estimation already clarified how the NMNI technique improves the Madgwick filter to diminish the drift and acquire a better angle. In this extensive work, the NMNI filter is fused with Mahony also then the comparison between both filter fusion is analyzed in detail. The Mahony computes the error by cross multiplying the measured and the estimated vectors to correct the gyroscope bias by the integral and proportional adjustable gains. Madgwick uses a gradient descent-based algorithm with an adjustable parameter divergent rate to correct the error.

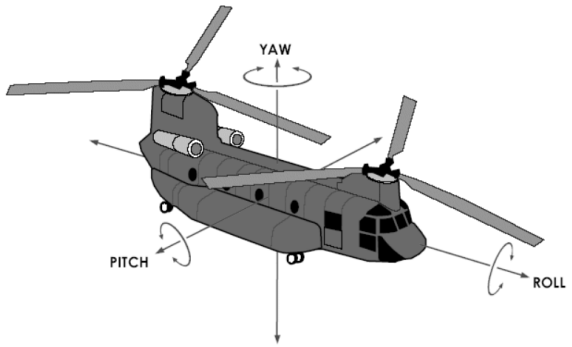

Fig. 1. Attitude example: roll, pitch and yaw angles on a helicopter. Picture taken from http://www.techmodelproducts.com/tandem_sw.htm

Each filter has its advantage and drawback respect to another filter. Therefore, numerous test was carried out to make a completed observation of filters. The static test was executed with a range from 10° to 90°; a comprehensive characterization of the start-up state, when the sensor stays at 0°, was executed. In addition to the dynamic test, a mixed motion test was used by combining static and dynamic behavior. Besides the setup for heading/yaw like before, an additional robust test bench was constructed on PTU for roll and pitch to be suitable with this device and attain the most precise angle tracking.

The paper is organized as follows: a brief description of Madgwick and Mahony are presented under no magnetometer mode, then the extended NMNI algorithms and its threshold update model are demonstrated. In the last section of this paper, test bench and result analysis are reported.

II. Sensor Fusion Algorithms

Before starting with a brief review of the Madgwick and Mahony filters, there is the need to define some fundamental quantities and sensors, measurement models.

The sensors used in Inertial Measurement Units (IMU) for orientation estimation and tracking are accelerometer, gyroscope, and magnetometer; the term MIMU (Magnetometer Inertial Measurement Unit) is used to distinguish between IMU with the three-axis magnetometer and the other platforms with only accelerometer and gyroscope. All three sensors are generally made with MEMS because of the low cost, reduced dimensions, low power consumption, but in particular for the simplicity, and they are integrated on PCBs (Printed Circuit Board) and in electronic devices in general. These sensors are differently affected by noise and measurement errors.

The magnetometer measures the magnetic field surrounding the device. This device is used to determine the heading of a moving object, cars, vehicles, ships, unmanned aerial vehicles, and even submarines. The measured field is highly affected by constant errors such as hard iron, soft iron, null shift errors, non-orthogonality, and scale factor errors and by time-varying errors caused by nearby fields produced by wires carrying high currents and electronics devices. The complexity and randomness of these errors require the development, implementation, and utilization of extended and time-consuming calibration procedures, error modeling and error compensation algorithms [20]–[22] to obtain high accuracy heading estimation. These algorithms are complex and require both time and power to be executed in embedded devices. In several industrial fields, such as robotic applications and high current motors, the magnetic fields generated by currents are strong enough to make the use of a magnetometer for the heading estimation impossible. In other cases, the heading evaluation does not represent a requirement. When this sensor is removed from the sensor fusion algorithm, a decrease in accuracy is obtained, and other tactics need to be applied to overcome this performance degradation.

The gyroscope measures the rate of change of the angle around the three axes of the sensing device. The measure of the gyroscope can be expressed as in (1) where w_x, w_y and w_z are the angular rate measured on each axis of the device.

$$\mathbf{w} = (w_x, w_y, w_z) \tag{1}$$

The measure of the gyroscope could be directly integrated to obtain an attitude estimation. This is not applicable because of the measurement errors of the gyroscope itself. The measurement is subject to a bias error, that models the gyroscope measure derivative by a random walk noise and an additive white noise.

The accelerometer measures the acceleration, which is composed of the sum of the gravity acceleration and body acceleration. The accelerometer measure can be expressed as in (2)

$$\mathbf{a} = (a_x, a_y, a_z) \tag{2}$$

As for the gyroscope, the measure made by the three-axial accelerometer is formed by the measurements on the three axes. The measurement is affected by additive white noise and a bias error modeled with Gauss-Markov noise.

A. Attitude representation and notation

The attitude represents the orientation of a body in the space. As can be seen in Fig. 1, using Euler angles, it is possible to define the following three quantities:

- the roll angle (ϕ), the rotation around the x-axis of the vehicle
- the pitch angle (θ) representing the rotation around a rotation around the y-axis
- the yaw angle (ψ) that corresponds to the rotation around the z-axis

Instead of Euler angles, quaternions are used for calculation of attitude filters. This representation form overcomes the problem of gimbal-lock and ambiguous representation of the Euler angles. A quaternion can be written as a vector with four elements (3).

$$q = (q_0, q_1, q_2, q_3) \tag{3}$$

Unit quaternions, all quaternions with a unit norm, can represent the attitude of a body. The definition of transformation goes beyond the scope of this article; more information about quaternions and Euler angles and rotation sequences can be found in [23], [24]. It is important to note that it is always possible to move from quaternion representation to Euler representation and vice-versa by using (4), (5) and (6).

$$\phi = \arctan \frac{q_0 q_1 + q_2 q_3}{q_0^2 - q_1^2 - q_2^2 + q_3^2} \tag{4}$$

$$\theta = \arcsin 2(q_1 q_3 - q_0 q_2) \tag{5}$$

$$\psi = \arctan \frac{q_1 q_2 + q_0 q_3}{1/2 - q_2^2 - q_3^2} \tag{6}$$

Notations of this paper are summarized in Table I.

TABLE I
NOTATIONS USED IN THIS PAPER FOR THE NMNI ALGORITHM

Notation	Meaning
$\omega[k]$	Gyroscope sample at discrete time k
$\omega_x[k], \omega_y[k], \omega_z[k]$	Gyroscope values on x, y, z axis respectively
ω_{bias}	Gyroscope bias value
ω_{th}	Gyroscope threshold value
$\hat{\omega}[k]$	Gyroscope measures after bias correction
$\omega^{\star}[k]$	Angular velocity from NMNI filter
ϕ, θ, ψ	Body attitude: roll, pitch and yaw angles

B. Madgwick Filter

The Madgwick filter is an Attitude and Heading Reference System (AHRS) algorithm, described clearly in [25], [26]. It uses the measured acceleration and magnetic field to correct for gyroscopic drift [27]. For the purpose of comparing performances with the proposed method, the Madgwick algorithms and its implementation will be briefly illustrated.

This sensor fusion technique is based on two estimates of the orientation: the angular velocity (gyroscope) with its previous orientation estimate and another on gradient descent-based algorithm for orientation estimate respect to gravity. This is a useful tool to fuse the accelerometer, gyroscope, and magnetometer every update step based on the quaternion [28]–[30].

The gyroscope measures the angular rate $\omega_x, \omega_y, \omega_z$ (in $rads^{-1}$), respect to the $x,\ y,\ z$ axes of the sensor frame, represented in s_ω in the quaternion form.

$$s_\omega = [0,\ \omega_x,\ \omega_y,\ \omega_z] \tag{7}$$

Given ${}^S_E\hat{q}$ as the vector describing the estimated orientation of *earth frame* relative to the *sensor frame* in the term of quaternion it can be expressed as in (8).

$${}^S_E\hat{q} = [q_0,\ q_1,\ q_2,\ q_3] \tag{8}$$

The derivative of the quaternion in (8) is ${}^S_E\dot{q}$ (9), it describes the rate of change of orientation of the earth frame relative to the sensor frame, used as calculation of the quaternion product between ${}^S_E\hat{q}$ and the gyroscope measures S_ω.

$${}^S_E\dot{q} = \frac{1}{2}{}^S_E\hat{q} \otimes s_\omega \tag{9}$$

The orientation of the earth frame relative to the sensor frame at time t is defined as ${}^S_E\dot{q}_{\omega,t}$ while $\omega_{S,t}$ represents the angular rate at time t.

Given ${}^S_E\dot{q}_{t-1}$ as the estimate of ${}^S_E q_{\omega,t}$ at time $t-1$, the quaternion $q_{\omega,t}$ and its derivative $\dot{q}_{\omega,t}$ can be calculated as in (10) and (11).

$$\begin{aligned} {}^S_E q_{\omega,t} &= {}^S_E\hat{q}_{t-1} + {}^S_E\dot{q}_{\omega,t}\Delta t && (10)\\ {}^S_E\dot{q}_{\omega,t} &= \tfrac{1}{2}{}^S_E\hat{q}_{t-1} \otimes s_{\omega,t} && (11) \end{aligned}$$

The accelerometer and magnetometer reading values are represented in quaternion space as in (12) and (13).

$$\begin{aligned} s_a &= [0,\ a_x,\ a_y,\ a_z] && (12)\\ s_m &= [0,\ m_x,\ m_y,\ m_z] && (13) \end{aligned}$$

The Madgwick calculation can be divided into four main steps, described below, supposing continuous-time t.

Step 1 - The first step is the calculation of rate of change δq. The variation of the quaternion is calculated using its estimation, as in (14).

$$\begin{aligned} \delta q &= \frac{1}{2}{}^S_E\dot{q} \otimes s_\omega = \\ &= \frac{1}{2}\begin{bmatrix} -q_1\omega_x - q_2\omega_x - q_3\omega_z \\ q_0\omega_x + q_2\omega_z - q_3\omega_y \\ q_0\omega_y - q_1\omega_z + q_3\omega_x \\ q_0\omega_z + q_1\omega_y - q_2\omega_x \end{bmatrix} \end{aligned} \tag{14}$$

Step 2 - A corrective step computation δq based on gradient descent algorithm is performed. Two reference vectors E_a and E_m, respectively for acceleration and magnetic field, are used to correct the deviation of the algorithm. The acceleration reference vector is defined in (15).

$$E_a = [0,\ 0,\ 0,\ g] \tag{15}$$

where g is the acceleration due to gravity ($g = 9.8\,\mathrm{m\,s^{-2}}$). Instead, if there are no magnetic deviations, then the magnetic reference vector E_m can be calculated as described in [31], [32]. The correction is calculated thanks to the Jacobian matrix J_t of the function F_t (16) that calculates the error of the projection of rotation on the reference acceleration vector E_a and magnetic reference vector E_m at time t given the acquired value of acceleration $s_{a,t}$ and magnetic field $s_{m,t}$.

$$F_t = \begin{bmatrix} {}^S_E q^{-1}_{t-1} \otimes E_{a,t} \otimes {}^S_E q_{t-1} - s_{a,t} \\ {}^S_E q^{-1}_{t-1} \otimes E_{m,t} \otimes {}^S_E q_{t-1} - s_{m,t} \end{bmatrix} I \tag{16}$$

$$\delta s = \frac{J_t^T F_t}{\|J_t^T F_t\|} \tag{17}$$

Step 3 - The quaternion change rate δq can be corrected with δs, calculated in (17), and integrated as follows.

$$\begin{aligned} \delta q' &= \delta q - \beta\delta s && (18)\\ \dot{q} &= \delta q' && (19)\\ q_t &= q_{t-1} + \delta q'\Delta t && (20) \end{aligned}$$

In (18) β is the divergence rate, a parameter that can be defined experimentally, based on the consideration in [19].

Without a magnetometer, the Madgwick filter cannot provide a proper result of yaw because of the large drift from the gyroscope [25].

C. Mahony filter

The main idea behind the Mahony filter is to correct the rotation vector S_ω with a correction vector, which is provided by a Proportional Integral (PI) controller [33]. The error vector $\mathbf{e}$ driving the PI controller is determined by the equation (21), where $\mathbf{a}$ is the accelerometer vector and $\mathbf{d}$ is the direction of the gravity vector as given by the estimated attitude.

$$\mathbf{e} = \mathbf{a} \times \mathbf{d} \tag{21}$$

Naming K_i and K_p as the integral and proportional adjustable gains, respectively, the Mahony algorithm can be divided into the following steps.

Step 1 - Estimation of gravity vector $\mathbf{d}$ from quaternion

$$\mathbf{d} = 2 \begin{bmatrix} q_1 q_3 - q_0 q_2 \\ q_0 q_1 + q_2 q_3 \\ {q_0}^2 + {q_3}^2 - 1/2 \end{bmatrix} \tag{22}$$

Step 2 - Error vector calculation

$$\mathbf{e} = \mathbf{a} \times \mathbf{d} \tag{23}$$

Step 3 - Integrative vector calculation

$$\mathbf{I}_n = \mathbf{I}_{n-1} + \mathbf{e} K_i \Delta t \tag{24}$$

Step 4 - Proportional vector

$$\omega^{'} = \omega + K_p \mathbf{I}_n \tag{25}$$

Step 5 - Integrate rate of change.

$$\mathbf{q}_n = \mathbf{q}_{n-1} + \dot{\mathbf{q}} \Delta t \tag{26}$$

Generally, increasing K_p will improve the system response to noise. However, if the Kp is too large, the process variable will begin to oscillate, causing unstable control. The integral component sums the error term over time. The result is that even a small error term will cause the integral component to increase slowly. The effect of the integral response is to drive the steady-state error to zero. Small values of K_i are used for small error term. If K_i is too large, the integral action saturates the controller; without the controller driving the error signal toward zero. In the last case, the system will be out of control.

III. 'No Motion No Integration' Algorithm

In order to compensate for bias instability, after the gyroscope is powered on, the MEMS gyroscope is in a stationary position, N samples are collected in an array W, and then averaged as the turn-on zero-rate level ω_{bias}. All the subsequent gyroscope readings can then subtract this turn-on zero-rate level as signed integers.

$$\omega_{bias} = \frac{1}{N} \sum_{i=0}^{N} \omega_i \tag{27}$$

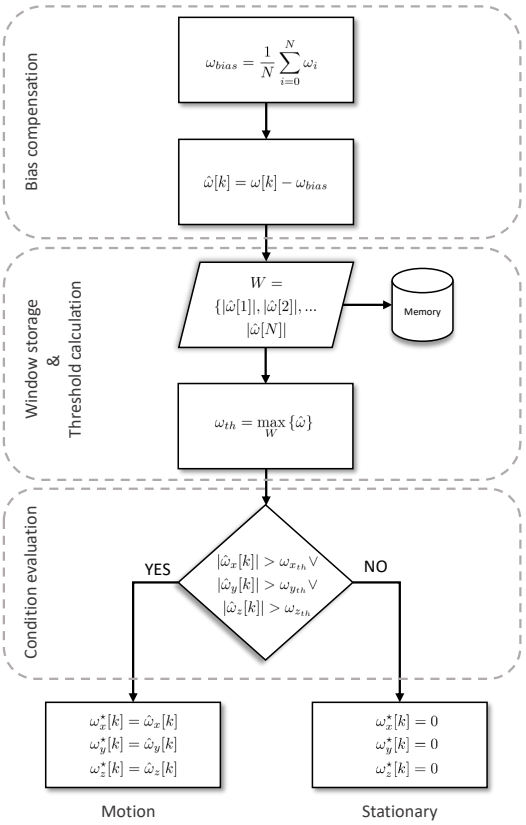

Fig. 2. Overview of NMNI algorithm.

All the subsequent gyroscope readings $\omega[k]$ must be then subtracted with turn-on zero-rate level defined in (27):

$$\hat{\omega}[k] = \omega[k] - \omega_{bias} \tag{28}$$

Once the initial bias is calculated, all the subsequent values will be appropriately integrated. After the initial phase, when the sensor stops its motion, the gyro data will be considered zero due to the NMNI filter. In Fig. 2, a block diagram representation of the whole NMNI algorithm is reported. This figure shows the idea of no integration portion added to the measuring value when the sensor finishes its movement.

A. NMNI technique

The gyroscope can be used to calculate the attitude angles yaw, pitch, and roll by integrating the angular rate from the x, y, z axis measurements $\omega_x, \omega_y, \omega_z$. Due to the temperature change, measurement noise, and drift problem, MEMS gyroscope readings will vary considerably even if the gyroscope stays at rest. Due to integration, the obtained results drift away from the range of real angle estimation. In the bad cases, the computed result can drift down of about $50°$ after 30 seconds [34].

For that reason, the idea of NMNI is carried out. No rotational rate is integrated to the orientation angle without

dynamic motion and only allows the integration process to continue when the sensor receives the next motion. Thus, a threshold must be established for the system realization whether the sensor is stopped or moved.

During the start-up phase, supposing that the body and the device are not subject to any motion, three arrays of a pre-fixed number of samples are filled with the absolute value of the measurements among the x, y, z axis. This phase is essential for the threshold setup; if the static condition is not met during start-up, the sample collection shifts in time. This process is done by controlling the acquired values and comparing them with a limit value ω_{max} defined, the first time the algorithm is run, as a user constant then it automatically updates with the threshold update model. The NMNI algorithm calculates the threshold value $\omega_{x_{th}}, \omega_{y_{th}}, \omega_{z_{th}}$ as the maximum between the absolute value of the acquired samples $\omega_x[i], \omega_y[i], \omega_z[i]$ as in ((29), (30), (31)).

$$\omega_{x_{th}} = \max_i \{|\omega_x[1]|,\ |\omega_x[2]|,\ ...,\ |\omega_x[i]|\} \tag{29}$$

$$\omega_{y_{th}} = \max_i \{|\omega_y[1]|,\ |\omega_y[2]|,\ ...,\ |\omega_y[i]|\} \tag{30}$$

$$\omega_{z_{th}} = \max_i \{|\omega_z[1]|,\ |\omega_z[2]|,\ ...,\ |\omega_z[i]|\} \tag{31}$$

The threshold values X_{th}, Y_{th}, Z_{th} become the boundary between static and dynamic circumstances. Besides the threshold values, a maximum value is extracted from the three vectors; this value is called ω_{gy}. Also a global threshold value, ω_{th}, is obtained as the maximum between the three values (32).

$$\omega_{th} = \max \{\omega_{x_{th}}, \omega_{y_{th}}, \omega_{z_{th}}\} \tag{32}$$

This value becames the overall bundary between the static and dynamic conditions. The principle works on the comparison between real-time measured $\omega[k]$ and threshold value ω_{th}:

- $|\hat{\omega}_x[k]| > \omega_{x_{th}}, \rightarrow$ roll is in rotation
- $|\hat{\omega}_y[k]| > \omega_{y_{th}}, \rightarrow$ pitch is in the dynamic rotation
- $|\hat{\omega}_z[k]| > \omega_{z_{th}}, \rightarrow$ yaw is in the dynamic rotation
- $|\hat{\omega}[k]| \leq \omega_{th} \rightarrow$ sensor is in the static case

At this point, the challenge is about the variation of gyroscope characteristics due to external factors like thermal change caused by temperature [35]. Therefore, the $\omega_{z_{th}}$ must be updated in the real-time term instead of measuring during a fixed period, as described in part III-B of this section.

B. Implementation

The implementation of the 'No Motion No Integration' algorithm, shortly NMNI, can be divided into two parts.

1) The first part used to calculate sensor offset ω_{bias} like an early mention, which can be seen as an array of N elements (optional number of samples).
2) The second part aimed to collect ω_{th} and acquisition $\hat{\omega}[k]$ at the current time; this second array has a size of W.

These two parts correspond to the parts in which the array structure, stored in memory, is divided. The overall reserved size of the acquisition array will be:

$$\text{Array Size} >= W + N \tag{33}$$

This size must be multiplied by three, for the number of axis involved in the calculation. Depending on the desired average time, the array size needs to be extended by the user: the greater the array size for a longer time, the gyroscope has to be at stationary. If the array size is too small, the system will be lack data to calculate ω_{th}.

For instance, considering the z axis, the $\omega_{z_{th}}$ value is stored at index 11 of the array, while the 12$^{\text{th}}$ element always indicates the current value of $\omega_{z_{th}}$; the same applies for the other axes, too. With this technique, the real-time comparison is instituted between $|\hat{\omega}_z[k]|$ and $\omega_{z_{th}}$.

C. Threshold Update

To guarantee the system's stability, each time the system is detected to be in a stationary position, a new threshold value is calculated and stored. If the new gyroscope acquisition has the absolute value (abs) higher than the current threshold, it will become the new threshold. This upgrade is necessary for long-term performance when sensor temperature increases, which causes the rise of gyroscope offset. However, to avoid the noise, the threshold only updated in the case of difference between abs of angular rate and the current threshold is smaller than angular rate sensitivity (ARS), which is up to the specifications of each gyroscope. The slowest motion leads to the variation of the least significant bit (LSB) and 1 LSB $\approx$ ARS. At stationary point, if $|\hat{\omega}[k]| > \omega_{th}$ and $|\hat{\omega}[k]| - \omega_{th} < \texttt{ARS}$ then $\omega_{th} = |\hat{\omega}[k]|$.

At this point, the suggested approach appears to incorporate standard procedure of removing the initial gyro bias (ignoring the Earth rotation), and an adaptive threshold filter applied to gyroscope measurements before integration that prevents any single drift portion from accumulation.

D. NMNI integration with Madgwick or Mahony filters

The NMNI is a preprocessing techique and can be applied to a attitude and heading reference estimation algorithm like Mahony or Madgwick in order to obtain device or body orientation. As depicted in Fig. 3, before entering the Madgwick or Mahony filter, the gyroscope data pass through the NMNI filter.

- $\hat{\omega}[k] > \omega_{th}$ the sensor is in motion: $\omega_x^\star, \omega_y^\star, \omega_z^\star$ come in the Madgwick or Mahony filter normally.
- $\hat{\omega}[k] \leq \omega_{th}$ the sensor is stationary: $\omega_x^\star, \omega_y^\star, \omega_z^\star$ assumes a zero value before entering the desired filter.

This fusion technique overcomes the dynamic integration problem on the slope of the NMNI filter and the random drift of the Madgwick or Mahony filter without a magnetometer.

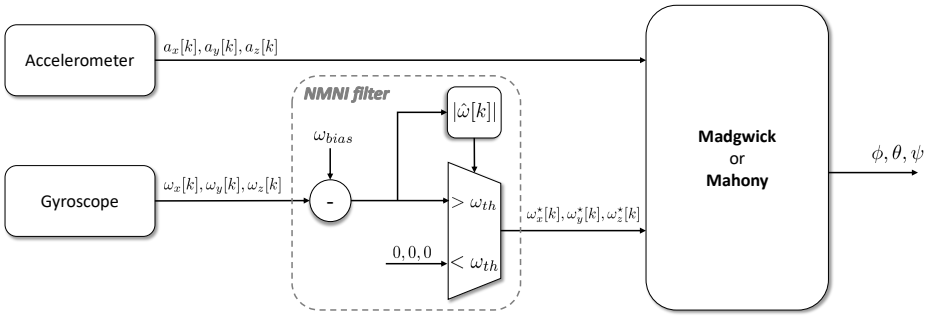

Fig. 3. Chain diagram of the fusion between Madgwick or Mahony and the NMNI filter.

IV. Experimental Results Analysis

The sensor involved in acquiring data for the experiments is the LSM9DS1 from *STMicroelectronics*. This device is a system-in-package featuring a tri-axial digital linear acceleration sensor with 16 bit resolution and selectable full-range scale from $\pm 2\,\mathrm{g}$ to $\pm 16\,\mathrm{g}$, a 3D digital angular rate sensor with 16 bit resolution and a full range scale of $\pm 245\,\mathrm{dps}$, $\pm 500\,\mathrm{dps}$ and $\pm 2000\,\mathrm{dps}$ the device also includes a 16 bit tri-axial magnetic sensor with selectable full-scale range of $\pm 4\,\mathrm{gauss}$, $\pm 8\,\mathrm{gauss}$, $\pm 12\,\mathrm{gauss}$ and $\pm 16\,\mathrm{gauss}$ [36].

The implementation of the algorithms has been made on an ARM Cortex-M4 based microcontroller STM32F401RE by STMicroelectronics [37], [38]. This device provides $96\,\mathrm{kB}$ of RAM and $512\,\mathrm{kB}$ of embedded programmable FLASH memory; the clock frequency is up to $84\,\mathrm{MHz}$. The MCU is mounted on its development board ST NUCLEO-F401RE [39], [40], for easy accessibility to all the required connections.

The sensor is mounted on the STEVAL-MKI159V1 adapter board [36] and connected to the MCU development via an Inter-Integrated Circuit (I_2C) communication line. A Pan-Tilt Unit Controller (PTU-C46), with a resolution $0.051°$ per step, provides fast and accurate positioning of sensors that were manipulated to verify the algorithm performance. The LSM9DS1 mounted on PTU-C for tracking this device orientation. For the evaluation of roll and pitch, the setup is modified, and PTU is mounted on the laboratory table vertically, as shown in Fig. 4. LSM9DS1 sensor assembled on a Printed Circuit Board with the support of a long cable to handle the controlled motion comfortably without any restrained problem.

The test bench reported in Fig. 4 is formed by the following components:

1) NUCLEO-F401RE Board
2) LSM9DS1 Sensor mounted on a Printed Circuit Board
3) Counterweight for balance
4) AC/DC Power Supply
5) RS232 cable
6) PTU-C Controller
7) PTU-C46 Pan Tilt Unit
8) Heavy duty clamps

The Output Data Rate (ODR) of the accelerometer and gyroscope was set at 119 Hz, equivalent to 0.008 s of the time period, to achieve a stable transferring signal between the sensor and the computer. Also, the magnetometer ODR is 80 Hz, about 0.0125 s of the period. Hence, the system acquisition carried out at 119 Hz for the filter without magnetometer and at 80 Hz vice versa. After many simulations with adjustable parameters, the best value of each algorithm factor for the experiment was chosen, taken into account the effective compromise among all Euler angles as follow:

- Madgwick: β = 0.40.
- Mahony: $K_p = 0.7$; $K_i = 0.002$
- ARS = 0.00875 deg/s

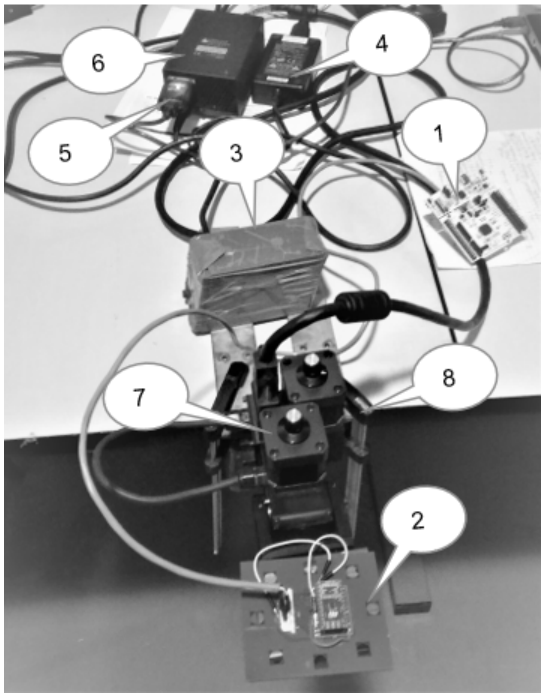

Fig. 4. Photograph of the test bench used for orientation measurement.

A. Filter behavior analysis and characterization

In the first part, the NMNI filter's function was examined on the yaw measurement, calculated by Madgwick and Mahony without a magnetometer. The sensor was kept at a stationary point approximately $0°$ for a minute to observe the drift of the result as well as the behavior of the algorithm.

As shown in Fig. 5, the yaw drift of Madgwick is very fast, and when it reached the $-180°$, it flips to $180°$ just after less than a minute. Due to the uncontrollable drift, the Madgwick algorithm without a magnetometer cannot be used for yaw estimation [16]. Therefore, to restraint this drift, the NMNI algorithm is the right solution as the first filter of gyroscope data before arriving Madgwick filter. As a result, the yaw is under control, indicating the appropriate behavior when the sensor is fixed at a position. The Madgwick filter performance was clearly improved after the fusion filter; the yaw value is maintained regularly at the stationary point, as shown in Table II. After optimization, the variation is minimized apparently and shows stable behavior.

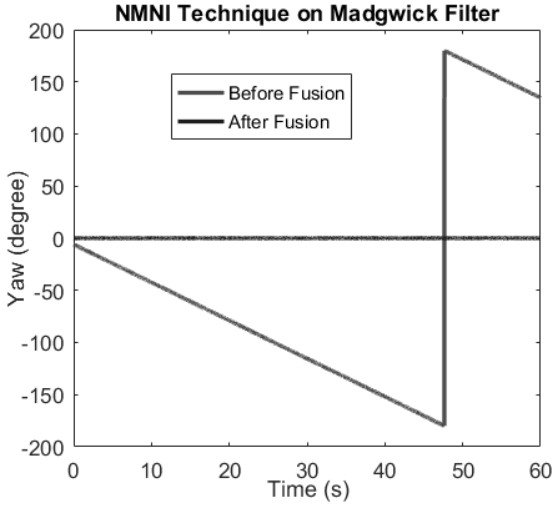

Fig. 5. Madgwick filter, without magnetometer, static drift before and after fusion.

TABLE II
MADGWICK DRIFT WITHOUT MAGNETOMETER BEFORE AND AFTER FUSED WITH NMNI ALGORITHM UNDER STATIC CONDITION

Yaw drift	Before Fusion	After Fusion
min	5.9°	0.010°
max	179.9°	0.064°
mean	39.8°	0.041°
std. dev.	111°	0.007°

The same progress carried out as fused Madgwick, the filter fusion with the NMNI upgrades the performance of Mahony yaw considerably. As illustrated in Fig. 6, Mahony yaw drifts down approximately $1\,\mathrm{dps}$, and it only behaves in the right way after fusion at the static point.

For the case of fused Madgwick and fused Mahony, the small variation still occurs on heading estimation due to the acceleration components. As observed results from Table

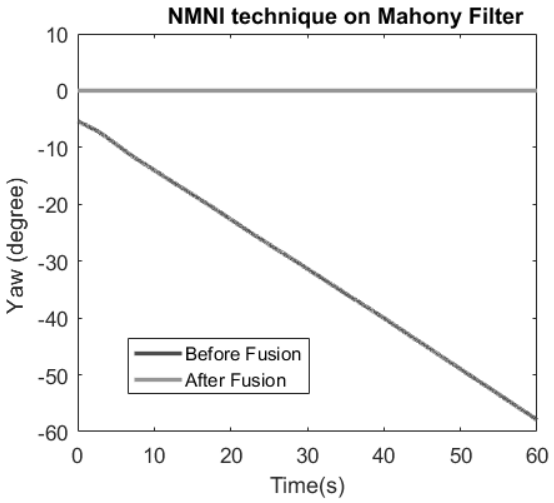

Fig. 6. Mahony static drift (no magnetometer) before and after fusion.

TABLE III
MAHONY DRIFT BEFORE AND AFTER FUSED WITH NMNI ALGORITHM UNDER STATIC CONDITION

Yaw drift	Before Fusion	After Fusion
min	5.3°	0.170°
max	57.9°	0.202°
mean	31.4°	0.175°
std. dev.	15.0°	0.031°

II and Table III, the NMNI works more effectively on the Madgwick filter with less fluctuation of the signal.

Fig. 7 and Fig. 8 shows the behavior of roll and pitch before and after applying the NMNI pre-processing technique. The signal is more stable with narrow variation in the fused filters. The fused Mahony filter keeps the signal smoother than the Fused Madgwick filter with an extremely small value of drift.

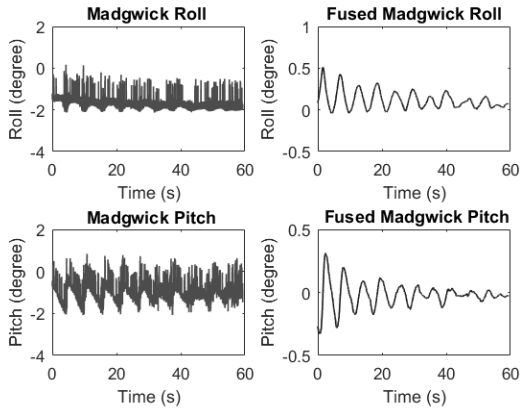

Fig. 7. Madgwick Roll and Pitch at zero-starting point.

With reference to Fig. 7 and Fig. 8 the result analysis of roll and pitch are reported in Tables IV and V, respectively. Roll is the parameter which is more influenced by drift than pitch in both cases. Thanks to the support of the fusion process, these

TABLE IV
MADGWICK ROLL AND PITCH BEFORE AND AFTER FUSED WITH NMNI ALGORITHM UNDER STATIC CONDITION

Abs Drift Parameters	Stand alone		Fused	
	Roll	Pitch	Roll	Pitch
min	0.13°	0.01°	−0.01°	0.002°
max	2.13°	2.07°	0.51°	0.329°
mean	1.68°	0.99°	0.12°	0.068°
std. dev.	0.30°	0.38°	0.10°	0.071°

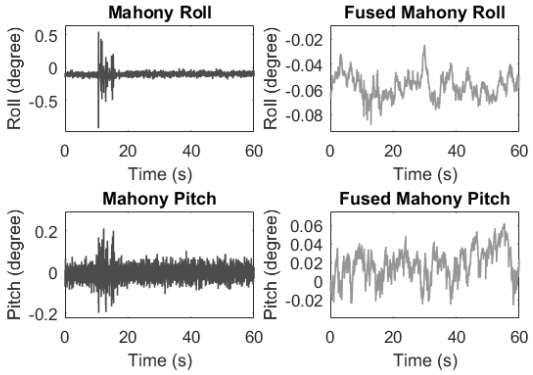

Fig. 8. Mahony Roll and Pitch at zero-starting point.

two Euler angles accomplish optimized drift with Standard Deviation (Std. Dev) only less than 0.11° for the Madgwick filter and 0.02° for the Mahony filter.

B. Static Tests

For the static test, the PTU is controlled from 0° to 90° with a different step of 10°, all acquired samples for a minute were extracted from each angle to calculate the Root Mean Square Error (RMSE). Fig. 9 shows the performances of two fused filters at Euler angles of 50°. Like in the static case, less drift occurs on the roll and pitch of Mahony filter, respect to Madgwick filter. About yaw estimation, the Mahony filter demonstrates a less effective tracking with error more than 0.232° while Madgwick yaw is closer to the reference angle of 50°.

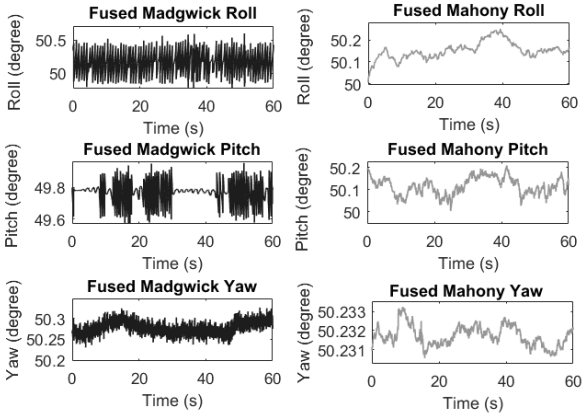

Fig. 9. Euler angles tracking at 50°.

TABLE V
MAHONY ROLL AND PITCH BEFORE AND AFTER FUSED WITH NMNI ALGORITHM UNDER STATIC CONDITION

Abs Drift Parameters	Stand alone		Fused	
	Roll	Pitch	Roll	Pitch
min	0.002°	0.004°	0.024°	0.003°
max	0.923°	0.210°	0.088°	0.062°
mean	0.099°	0.026°	0.057°	0.020°
std. dev.	0.040°	0.022°	0.009°	0.013°

A similar process was carried out to other considerable angles. Generally, a larger angle conducts higher RMSE as a result of Table VI. Both fused Madgwick and fused Mahony show a convincing result. The fused Mahony filter accomplishes better performance in the roll and pitch, but the fused Madgwick achieves more stable in yaw measurement with maximum RMSE only less than 0.4°.

TABLE VI
STATIC TESTS RMSE ANALYSIS OF FUSED MADGWICK AND MAHONY FILTERS

Reference	Madgwick RMSE			Mahony RMSE		
	Roll	Pitch	Yaw	Roll	Pitch	Yaw
10°	0.112°	0.167°	0.082°	0.099°	0.051°	0.100°
20°	0.155°	0.137°	0.079°	0.156°	0.082°	0.124°
30°	0.247°	0.201°	0.105°	0.133°	0.117°	0.133°
40°	0.201°	0.198°	0.126°	0.184°	0.159°	0.135°
50°	0.184°	0.233°	0.177°	0.152°	0.117°	0.231°
60°	0.340°	0.211°	0.281°	0.271°	0.273°	0.342°
70°	0.290°	0.269°	0.346°	0.267°	0.258°	0.511°
80°	0.258°	0.331°	0.379°	0.311°	0.259°	0.378°
90°	0.351°	0.322°	0.381°	0.279°	0.270°	0.527°

C. Dynamic Test

For the test of the dynamic test, the device PTU-C was moved from 0° to 90° back and forth for a minute like described in the previous article [19].

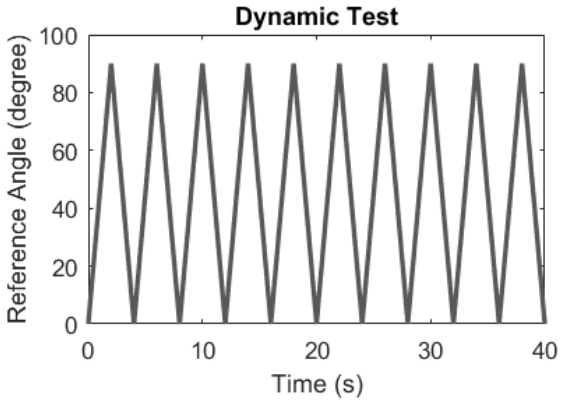

Fig. 10. Test reference for dynamic case.

Each time the PTU-C reaches the edged points: 0° or 90°, this device is in stillness in an extremely short period of time due to inertia, which is the resistance of a physical object to change in its direction of motion. This period is very critical because even just a small drift portion occurs at this

moment, the errors would accumulate and yield the incorrect measurement. Therefore, the NMNI filter must be exact to eliminate these drift portions. The PTU-C rotates ten turns back and forth at velocity $45\,\mathrm{dps}$ as demonstrated in Fig. 10. RMSE calculates the data evaluation in Table VII. Under this stressful test, the fused Madgwick filter has a stable result among roll, pitch, and yaw. All these parameters only have RMSE around $0.4°$, while the fused Mahony conducts more error at heading estimation, but it still shows its potential accuracy in orientation tracking.

TABLE VII
RMS ERROR OF THE DYNAMIC TEST ON FUSED MADGWICK AND MAHONY

Euler Angle	Fused Madgwick	Fused Mahony
Roll	$0.403°$	$0.355°$
Pitch	$0.370°$	$0.401°$
Yaw	$0.402°$	$0.589°$

The test of mixed motion, Fig. 11 includes both static and dynamic behavior. Each cycle has a shape of a trapezoid. Similar to the previous test, the PTU moves from $0°$ to $90°$ but instead of returning to $0°$ immediately, the device holds at $90°$ for $3\,\mathrm{s}$ before going down. At this point, the cumulative error to consider will be evaluated in the completed way.

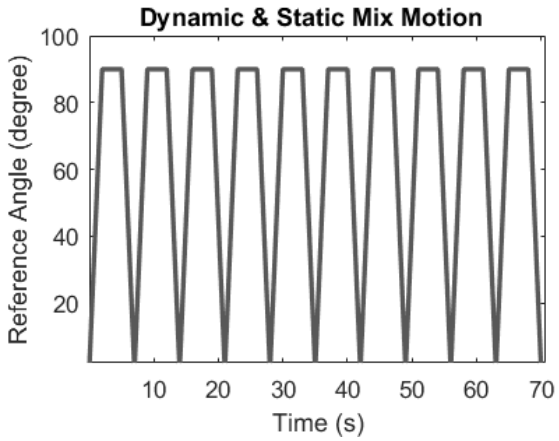

Fig. 11. Test reference for mixed motion test case.

Table VIII indicates the good tracking capability of two fused filters. In this test, filters have a longer static where the threshold can update more easily and do not have to suffer the collision frequently. Each time PTU reaches $90°$, if it must return to $0°$, it will generate a vibration to mimic dynamic continuous motion.

TABLE VIII
RMS ERROR UNDER MIXED MOTION ON FUSED MADGWICK AND MAHONY

Euler Angle	Fused Madgwick	Fused Mahony
Roll	$0.275°$	$0.214°$
Pitch	$0.302°$	$0.209°$
Yaw	$0.202°$	$0.207°$

D. Temperature behavior

To observe the behavior of the oriental angles during the temperature variation a smart experiment was carried out on the Earth frame. The temperature of the sensor was increased in the range of $25\,°\mathrm{C}$ to $40\,°\mathrm{C}$ with the help of heat air flux. The temperature was measured with the embedded temperature sensor in LSM9DS1 module. For each temperature step, 50 samples were extracted for the mean value calculation.

As shown in the Fig. 12, the orientation value of the fused Mahony filter and the fused Madgiwck filter have high stability under the temperature change. The maximum fluctuation of the fused Madgwick filter is only about $0.080°$ at $40\,°\mathrm{C}$. On the other hand, the Mahony filter demonstrates better immunity in temperature variation with smaller alterations in all Euler angles.

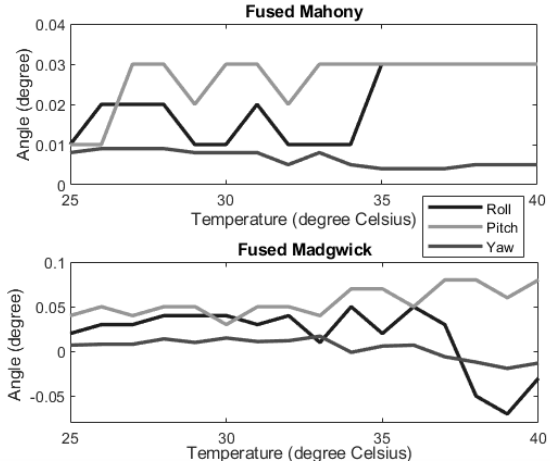

Fig. 12. Test reference for temperature variations.

V. CONCLUSION

In this paper, the development of a filter algorithm with the optimization of the NMNI technique is reported. The experimental results verify the significant improvement of Mahony and Madgwick filter in orientation tracking thanks to the proposed pre-processing model. The fused Madgwick is strongly recommended for heading and yaw estimation, while the fused Mahony can track roll and pitch at closer reference angles with less drift and high precision.

The real-time measurement has been completed so far via tests of static-dynamic-mixed motion. Both filters, when fused with the NMNI technique, have a good command of detecting the inclination as well as heading with narrow errors and high stability during operation. The variation due to temperature are kept at minimum level. The NMNI technique is a promising collaborator with other sensor fusions methods via effectiveness maximization for the gyroscope.

REFERENCES

[1] M. Carratú, S. Dello Iacono, M. Hoang, and A. Pietrosanto, "Energy characterization of attitude algorithms," in *IEEE International Conference on Industrial Informatics, INDIN19*, 2019, pp. 1585–1590.

[2] A. Harindranath and M. Arora, "Mems imu sensor orientation algorithms-comparison in a simulation environment," in *2018 International Conference on Networking, Embedded and Wireless Systems (ICNEWS)*, Dec 2018, pp. 1–6.

[3] B. Huyghe, J. Doutreloigne, and J. Vanfleteren, "3d orientation tracking based on unscented kalman filtering of accelerometer and magnetometer data," in *2009 IEEE Sensors Applications Symposium*, 2009, pp. 148–152.

[4] G. Lan, Y. Bu, J. Liang, and Q. Hao, "Action synchronization between human and uav robotic arms for remote operation," in *2016 IEEE International Conference on Mechatronics and Automation*, 2016, pp. 2477–2481.

[5] X. Kong, "INS algorithm using quaternion model for low cost IMU," *Robotics and Autonomous Systems*, vol. 46, no. 4, pp. 221–246, 2004.

[6] G. Qinglei, L. Huawei, M. Shifu, and H. Jian, "Design of a plane inclinometer based on mems accelerometer," in *2007 International Conference on Information Acquisition*, 2007, pp. 320–323.

[7] J. Wang, G. Gao, and P. Liu, "The study on lange-angle canbus 2-axis inclinometer of rotary drilling rig," in *2010 2nd IEEE International Conference on Information Management and Engineering*, 2010, pp. 95–97.

[8] L. Da-wei and G. Tao, "Design of dual-axis inclinometer based on mems accelerometer," in *2011 Third International Conference on Measuring Technology and Mechatronics Automation*, vol. 1, 2011, pp. 959–961.

[9] M. Lobur and A. Holovatyy, "Overview and analysis of readout circuits for capacitive sensing in mems gyroscopes (mems angular velocity sensors)," in *2009 5th International Conference on Perspective Technologies and Methods in MEMS Design*, 2009, pp. 161–163.

[10] H. D. Gavcar, K. Azgin, S. E. Alper, and T. Akin, "An automatic acceleration compensation system for a single-mass mems gyroscope," in *2015 Transducers - 2015 18th International Conference on Solid-State Sensors, Actuators and Microsystems (TRANSDUCERS)*, 2015, pp. 19–22.

[11] J. Bahari and C. Menon, "Exclusion of linear acceleration signal in the mems thermal gyroscope," *Journal of Microelectromechanical Systems*, vol. 27, no. 1, pp. 19–21, 2018.

[12] P. Minotti, S. Dellea, G. Mussi, A. Bonfanti, S. Facchinetti, A. Tocchio, V. Zega, C. Comi, A. L. Lacaita, and G. Langfelder, "High scale-factor stability frequency-modulated mems gyroscope: 3-axis sensor and integrated electronics design," *IEEE Transactions on Industrial Electronics*, vol. 65, no. 6, pp. 5040–5050, 2018.

[13] S. Sabatelli, M. Galgani, L. Fanucci, and A. Rocchi, "A double-stage kalman filter for orientation tracking with an integrated processor in 9-d imu," *IEEE Transactions on Instrumentation and Measurement*, vol. 62, no. 3, pp. 590–598, 2013.

[14] M. Euston, P. Coote, R. Mahony, J. Kim, and T. Hamel, "A complementary filter for attitude estimation of a fixed-wing uav," in *2008 IEEE/RSJ International Conference on Intelligent Robots and Systems*, 2008, pp. 340–345.

[15] M. Selvarajan and C. M. Ananda, "Quaternion based pointing algorithm for two-axis gimbal of micro aerial vehicles," in *2016 IEEE International Conference on Recent Trends in Electronics, Information Communication Technology (RTEICT)*, 2016, pp. 1335–1339.

[16] S. O. H. Madgwick, A. J. L. Harrison, and R. Vaidyanathan, "Estimation of imu and marg orientation using a gradient descent algorithm," in *2011 IEEE International Conference on Rehabilitation Robotics*, 2011, pp. 1–7.

[17] S. Yean, B. S. Lee, C. K. Yeo, and C. H. Vun, "Algorithm for 3d orientation estimation based on kalman filter and gradient descent," in *2016 IEEE 7th Annual Information Technology, Electronics and Mobile Communication Conference (IEMCON)*, 2016, pp. 1–6.

[18] S. A. Ludwig, "Optimization of control parameter for filter algorithms for attitude and heading reference systems," in *2018 IEEE Congress on Evolutionary Computation (CEC)*, 2018, pp. 1–8.

[19] M. L. Hoang, A. Pietrosanto, S. Dello Iacono, and V. Paciello, "Preprocessing technique for compass-less madgwick in heading estimation for industry 4.0," in *2020 IEEE International Instrumentation and Measurement Technology Conference (I2MTC)*, 2020, pp. 1–6.

[20] Z. Liu and M. Zhu, "Calibration and error compensation of magnetometer," in *The 26th Chinese Control and Decision Conference (2014 CCDC)*, 2014, pp. 4122–4126.

[21] R. Alonso and M. Shuster, "Twostep: A fast robust algorithm for attitude-independent magnetometer-bias determination," *The Journal of the Astronautical Sciences*, vol. 50, pp. 433–451, 10 2002.

[22] ——, "Complete linear attitude-independent magnetometer calibration," *The Journal of the Astronautical Sciences*, vol. 50, pp. 477–490, 10 2003.

[23] J. Diebel, "Representing attitude: Euler angles, unit quaternions, and rotation vectors," *Matrix*, vol. 58, 01 2006.

[24] J. B. Kuipers, *Quaternions and rotation sequences : a primer with applications to orbits, aerospace, and virtual reality*. Princeton, NJ: Princeton Univ. Press.

[25] S. O. H. Madgwick, A. J. L. Harrison, and R. Vaidyanathan, "Estimation of imu and marg orientation using a gradient descent algorithm," *IEEE International Conference on Rehabilitation Robotics : [proceedings]*, vol. 2011, p. 5975346, 06 2011.

[26] O. Sarbishei, "On the accuracy improvement of low-power orientation filters using imu and marg sensor arrays," in *2016 IEEE International Symposium on Circuits and Systems (ISCAS)*, 2016, pp. 1542–1545.

[27] M. Admiraal, S. Wilson, and R. Vaidyanathan, "Improved formulation of the imu and marg orientation gradient descent algorithm for motion tracking in human-machine interfaces," in *2017 IEEE International Conference on Multisensor Fusion and Integration for Intelligent Systems (MFI)*, 2017, pp. 403–410.

[28] H. Xing, Z. Chen, C. Wang, M. Guo, and R. Zhang, "Quaternion-based complementary filter for aiding in the self-alignment of the mems imu," in *2019 IEEE International Symposium on Inertial Sensors and Systems*, 2019, pp. 1–4.

[29] M. Selvarajan and C. M. Ananda, "Quaternion based pointing algorithm for two-axis gimbal of micro aerial vehicles," in *2016 IEEE International Conference on Recent Trends in Electronics, Information & Communication Technology (RTEICT)*, 2016, pp. 1335–1339.

[30] T. Brunner, J. Lauffenburger, S. Changey, and M. Basset, "Quaternion-based imu and stochastic error modeling for intelligent vehicles," in *2015 IEEE Intelligent Vehicles Symposium (IV)*, 2015, pp. 877–882.

[31] NGA and the U.K.'s Defence Geographic Centre (DGC). (2015) The world magnetic model. [Online]. Available: http://www.ngdc.noaa.gov/geomag/WMM

[32] S. A. Ludwig and K. D. Burnham, "Comparison of euler estimate using extended kalman filter, madgwick and mahony on quadcopter flight data," in *2018 International Conference on Unmanned Aircraft Systems (ICUAS)*, 2018, pp. 1236–1241.

[33] R. Mahony, T. Hamel, and J. Pflimlin, "Nonlinear complementary filters on the special orthogonal group," *IEEE Transactions on Automatic Control*, vol. 53, no. 5, pp. 1203–1218, 2008.

[34] F. Abyarjoo, A. Barreto, J. Cofino, and F. Ortega, "Implementing a sensor fusion algorithm for 3d orientation detection with inertial/magnetic sensors," in *Lecture Notes in Electrical Engineering*, vol. 313. Springer, 01 2012.

[35] S. Feng, G. Qiufen, G. Yuansheng, and L. Junshan, "Research on thermal characteristic in slow-small temperature changing for mems linear vibration gyroscope," in *2006 International Conference on Mechatronics and Automation*, 2006, pp. 475–479.

[36] *iNEMO inertial module: 3D accelerometer, 3D gyroscope, 3D magnetometer - Data Sheet*, STMicroelectronics, March 2015.

[37] *Ultra-low-power Arm® Cortex®-M4 32-bit MCU+FPU, 105 DMIPS, 512KB Flash/96KB RAM, 11 TIMs, 1 ADC, 11 comm. interfaces*, STMicroelectronics, January 2015.

[38] *STM32F401xB/C and STM32F401xD/E advanced Arm®-based 32-bit MCUs*, STMicroelectronics, December 2018.

[39] *STM32 Nucleo-64 boards - Product Specifications*, STMicroelectronics, October 2018.

[40] *STM32 Nucleo-64 boards - User Manual*, STMicroelectronics, December 2017.